

# Stable Spike: Dual Consistency Optimization via Bitwise AND Operations for Spiking Neural Networks

Yongqi Ding, Kunshan Yang, Linze Li, Yiyang Zhang, Mengmeng Jing, Lin Zuo\*  
 School of Information and Software Engineering  
 University of Electronic Science and Technology of China

## Abstract

*Although the temporal spike dynamics of spiking neural networks (SNNs) enable low-power temporal pattern capture capabilities, they also incur inherent inconsistencies that severely compromise representation. In this paper, we perform dual consistency optimization via **Stable Spike** to mitigate this problem, thereby improving the recognition performance of SNNs. With the hardware-friendly “AND” bit operation, we efficiently decouple the stable spike skeleton from the multi-timestep spike maps, thereby capturing critical semantics while reducing inconsistencies from variable noise spikes. Enforcing the unstable spike maps to converge to the stable spike skeleton significantly improves the inherent consistency across timesteps. Furthermore, we inject amplitude-aware spike noise into the stable spike skeleton to diversify the representations while preserving consistent semantics. The SNN is encouraged to produce perturbation-consistent predictions, thereby contributing to generalization. Extensive experiments across multiple architectures and datasets validate the effectiveness and versatility of our method. In particular, our method significantly advances neuromorphic object recognition under ultra-low latency, improving accuracy by up to 8.33%. This will help unlock the full power consumption and speed potential of SNNs.*

## 1. Introduction

The rapid development of deep learning, especially the emergence of large models, makes the power consumption of AI models a non-negligible challenge. The human brain, on the other hand, enjoys a significant power consumption advantage over artificial neural networks (ANNs) [32], making neuromorphic computing a promising low-power, high-performance computing paradigm [27]. Spiking neural networks (SNNs) transmit sparse binary spikes over multiple timesteps, requiring only addition operations when deployed on neuromorphic chips, and consuming signifi-

cantly less power compared to ANNs [46–48]. Similarly, neuromorphic data represents information as sparse binary events, and recognizing neuromorphic objects using SNNs can be inherently low-power and low-latency [5, 40, 48].

However, although temporal spike dynamics give SNNs low-power spatio-temporal representations, they also introduce the risk of inconsistency. Differences in neuronal states and input currents across timesteps lead to excessive variability in spike maps and predictions, negatively affecting overall performance [6]. To address this problem, [6] indirectly promotes spike consistency through membrane potential smoothing and maintains the overall stability by performing logit distillation with adjacent timesteps. Although effective, this indirect strategy requires the modification of neuronal dynamics and struggles to be readily adopted as a versatile SNN enhancement solution, especially for deployment on neuromorphic chips where neuron models are often predetermined [17, 26, 48]. Therefore, efficiently and versatily promoting the predictive consistency and performance of SNNs remains an open challenge.

In this paper, we propose the **Stable Spike**, which efficiently improves the consistency and performance of the SNN without any modification to the spiking neurons or architecture. Our method stems from a key insight: *despite differences, a well-optimized SNN can capture object-critical features at different timesteps*. This is illustrated by the spike map visualization in Fig. 1, where spike maps of different timesteps capture object-relevant features, while excessive redundant noise spikes unrelated to the object lead to variability. Therefore, we can decouple and extract the critical information, i.e. the stable spike skeleton, from the variational spike maps. To do this, we perform a hardware-friendly “AND” bit operation [29, 44] on the spike maps of adjacent timesteps to efficiently retrieve consistent and stable 1-value spikes while ignoring messy spikes. As shown in Fig. 1, the stable spike maps reduce variability and outline a clear feature skeleton. We encourage the original spike maps to converge to the stable spike during training, which directly reduces the discrepancy between the multi-timestep spike maps and mitigates the in-

\*Corresponding author (linzuo@uestc.edu.cn).

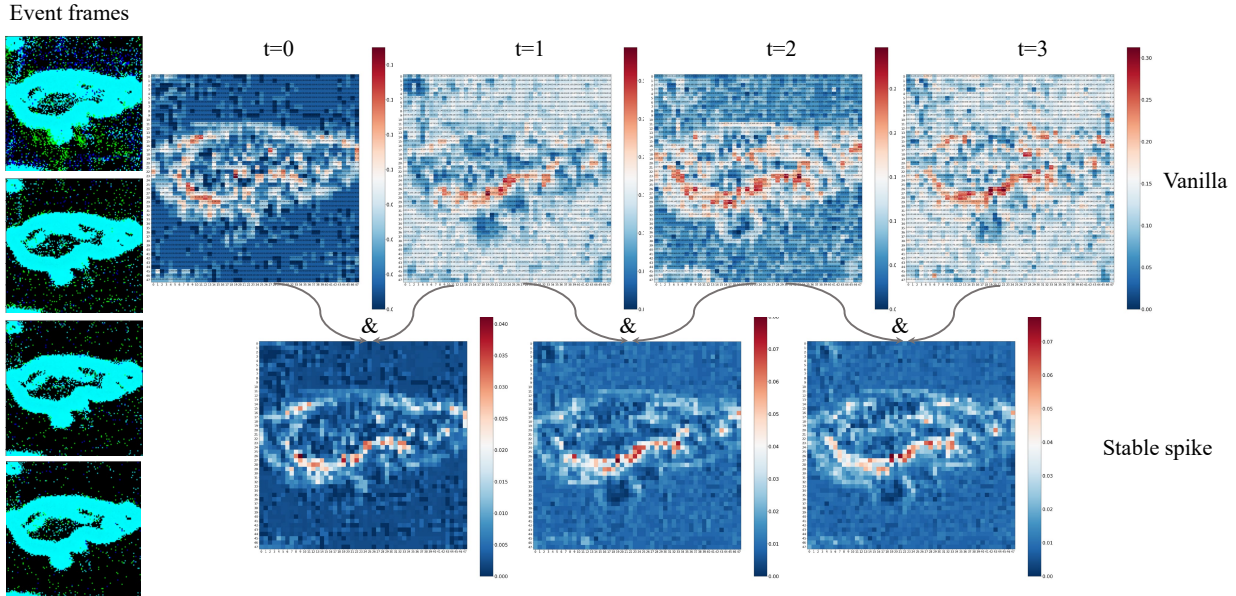


Figure 1. Comparison of vanilla SNN spike maps and stable spike maps. Vanilla spike maps varied widely across timesteps, negatively affecting the overall representation; stable spike maps, decoupled by minimal  $\&$  operation, consistently represented the feature skeleton. The event frames are from the CIFAR10-DVS dataset and the visualization shows the spike maps of the first layer in VGG-9 after averaging over all channels. Additional visualizations in **Supplementary Material** show that the stable spike consistently extracts the feature skeleton.

terference of redundant, varying noise spikes.

While consistency across timesteps stabilizes the overall prediction, moderate diversity promotes generalization and convergence [11, 22]. However, unlike ANNs that can directly benefit from random Gaussian noise [22], SNNs necessitate that (1) the noise to be discrete or else a mismatch in training-inference precision will occur, and (2) the noise amplitude to be appropriate or else it will interfere with normal training. To this end, we propose amplitude-aware spike noise, which possesses the discrete properties of binary spikes and generates noise depending on the amplitude of the spike firing rate. This enables the noise to adequately contribute to the generalization of high-amplitude elements while preventing low-amplitude elements from being overly perturbed. We inject amplitude-aware spike noise into the stable spike firing rate skeleton to preserve critical object semantics and push the perturbed predictions to approximate the original predictions. This enhances the perturbation consistency of SNNs to unknown variations, thereby improving generalizability.

Facilitated by dual consistency, our method efficiently boosts the performance of the SNN without changing the neurons or the model architecture. This allows our method to be plug-and-play for different spiking neurons and architectures, and to synergize with other methods to enhance performance (as shown in Table 9) with excellent versatility. In particular, our method significantly enhances performance on neuromorphic datasets, boosting the accuracy of DVS-Gesture by up to 8.33% under ultra-low latency at two timesteps. Our contributions are summarized below:

- We propose to decouple the stable spike feature skeleton across timesteps from the SNN by the efficient “AND” operation, and provide consistency guidance to the unstable spike maps.
- We propose to inject amplitude-aware spike noise into the stable spike firing rate to increase feature diversity and improve generalization by enhancing the perturbation prediction consistency of the SNN.
- Extensive experiments across multiple architectures and datasets demonstrate the effectiveness and versatility of our method, especially at enabling neuromorphic object recognition with ultra-low latency.

## 2. Related Work

**Spiking Neural Network.** SNNs mimic the information transfer mechanism of the biological nervous system, where binary spike signals are transmitted between spiking neurons over multiple timesteps [32, 40, 47]. Additionally, spiking neuron dynamics can capture implicit temporal dependencies, enabling SNNs to exhibit superior spatio-temporal properties [30]. This allows SNNs to be efficiently deployed on neuromorphic chips, providing performance comparable to that of ANNs while consuming substantially less power [46, 48]. Previous studies have focused on improving the neuron dynamics [9, 18], model architectures [38, 47, 54], and training algorithms [2] to unleash the potential of SNNs. However, the inconsistency of SNNs across timesteps remains an unsolved issue that limits their performance, especially at low latency. Although [6] modifies the neural dynamics and guides the output between

neighboring timesteps to alleviate this problem, further solutions that are more efficient and effective are still needed. To this end, this paper performs dual consistency optimization via the efficient stable spike, without any modification of neurons or architectures, and compatible with other improvements.

**Neuromorphic Object Recognition.** Unlike traditional static images, neuromorphic sensors such as event cameras represent data as sparse binary events with high temporal resolution and are able to capture motion information about the object [5, 23, 34]. The dimensionality of neuromorphic data can be denoted as  $[t, x, y, p]$ , where  $t$  is the temporal index,  $[x, y]$  are the spatial coordinates of the data, and  $p$  is the polarity (positive polarity indicates that pixel brightness has increased above a certain threshold, and negative polarity is the opposite). This spatio-temporal property makes neuromorphic objects naturally suited for recognition by SNNs, and the power and speed benefits of combining the two have been widely demonstrated [23, 48]. There has been extensive work on optimizing SNNs for neuromorphic object recognition, but they still suffer from significant latencies [2, 10, 25, 52] (typically more than 10 timesteps). In particular, [6] points out that the temporal instability of SNNs is particularly pronounced in neuromorphic data and is a bottleneck limiting their low-latency performance. For these reasons, this paper focuses on enhancing neuromorphic object recognition with SNNs at ultra-low latencies. But notice that, as demonstrated in the experimental section, our method is also effective for static data.

**Consistency in SNNs.** Inspired by ANNs, previous methods have improved the spatial feature consistency of SNNs through knowledge distillation [14, 42, 43] and contrastive learning [31, 53]. However, focusing solely on spatial aspects fails to leverage the spatio-temporal properties of SNNs fully, especially hindering their integration with neuromorphic data. To improve temporal consistency, especially in neuromorphic recognition performance, further studies distill the temporal dimension [7, 8, 57] or promote consistency in representations between neuromorphic and static objects [16]. However, while consistency has been facilitated, the lack of a stable anchor of consistency has limited the effectiveness of these methods. In this paper, we decouple the stable spikes that outline the feature skeleton as an anchor through the efficient ‘‘AND’’ operation, thus guiding the variable spike maps towards consistency.

### 3. Method

We first describe the spiking neuron dynamics and the inconsistency problem in SNNs, and then detail how dual consistency optimization can be efficiently achieved by stable spike to improve the performance of SNNs.

#### 3.1. Inconsistency Arising from Spike Dynamics

The spiking neuron is the core element in SNNs that mimics the biological charge-firing mechanism to generate binary spike signals. In this paper, we use the most commonly used leaky integrate-and-fire (LIF) neuron model [6, 41], which balances biological plausibility with ease of implementation. The LIF neuron model iteratively undergoes three phases of charging, firing, and resetting within  $T \geq 1$  discrete timesteps. Upon receiving an input current  $I$  from presynaptic neurons, the LIF neuron incorporates it into the membrane potential  $H$ , i.e., charging. The LIF neuron then determines whether the membrane potential exceeds a specific firing threshold  $\vartheta$  to generate a spike  $S$  or remain silent. During the resetting phase, the LIF neuron updates the membrane potential based on the fired spike, subtracting the membrane potential by the same amplitude as the threshold in a soft reset manner, and leaving it unchanged if no spike is fired. The iterative dynamics of LIF neurons within a single timestep can be expressed as:

$$H_{i,t}^l = (1 - \frac{1}{\tau})H_{i,t-1}^l + I_{i,t}^l, \quad (1)$$

$$S_{i,t}^l = \begin{cases} 1, & H_{i,t}^l \geq \vartheta \\ 0, & H_{i,t}^l < \vartheta \end{cases}, \quad (2)$$

$$H_{i,t}^l = H_{i,t}^l - S_{i,t}^l \vartheta, \quad (3)$$

where  $l$ ,  $i$ , and  $t$  denote the layer, neuron, and timestep indexes in the SNN, respectively. In particular, the membrane potential of LIF neurons leaks when the dynamics iterate to the next timestep, which is controlled by  $\tau$  in Eq. (1) with a default value of 2.0.

The output of a spiking neuron at each timestep depends on both the input  $I$  and its membrane potential value  $H$ , since the membrane potential is maintained across timesteps. The synergistic interaction of these two factors results in differences in the output of the SNN across timesteps. As shown in Fig. 1, excessive differences between spike maps across timesteps lead to overall inconsistency, and plenty of highly variable spurious spikes impeding semantic feature extraction. In particular, since the membrane potential of the spiking neuron is usually initialized to 0, the output of the early timestep is more confusing compared to the late one [6, 41]. The inconsistency across timesteps limits the overall performance of the SNN, especially when only early timesteps are available for low-latency inference.

#### 3.2. Stable Spike for Spike Map Consistency

To promote multi-timestep consistency of SNNs, we separate the variable spike feature maps into consistent stable spike skeletons and unstable spurious redundant spikes. Therefore, we are able to train the spike feature maps to converge to a stable and consistent skeleton while ignoring the interference of redundant and variable spurious spikes.

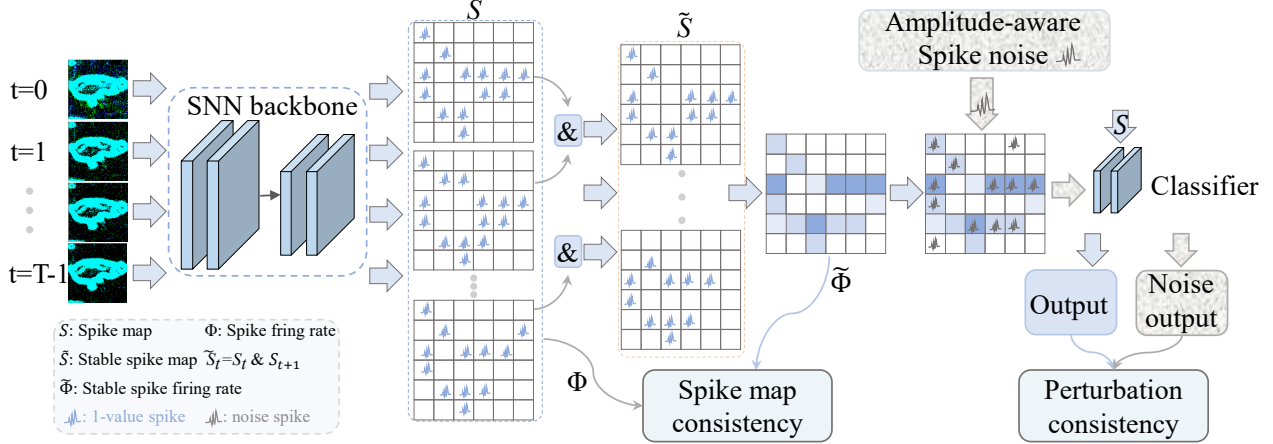


Figure 2. The stable spikes decoupled by the minimal  $\&$  operation are used as the anchor. On the one hand, we promote the variable original spike maps to converge to the stable spike firing rate skeleton, i.e., spike map consistency. On the other hand, we introduce amplitude-aware spike noise to the stable spiking firing rate to preserve the key semantics and increase the feature diversity, allowing the SNN to be insensitive to the perturbation and promote generalization, i.e., perturbation consistency.

Without loss of generality, we denote the spike feature map generated by the SNN over  $T$  timesteps as  $S \in \{0, 1\}^{T \times B \times C \times H \times W}$ , where  $B$  is the batch size,  $C$  is the number of channels, and  $H$  and  $W$  denote the height and width, respectively (temporarily ignore layer indices). To efficiently extract salient semantic features captured by the SNN over  $T$  timesteps from the unstable  $S$ , we use the binary data-friendly “AND” ( $\&$ ) operation to compute the stable spike skeleton between adjacent spike maps. In particular, the  $\&$  operation is able to preserve 1-valued elements coexisting in the two binary data while eliminating unstable noise elements, and is naturally suited for modeling consistency in SNNs. Among the  $T$  varying spike maps, we extract a total of  $T - 1$  stable spikes, which is expressed in mathematical form as follows:

$$\tilde{S}_{i,t} = S_{i,t} \& S_{i,t+1} = \begin{cases} 1, & S_{i,t} = S_{i,t+1} = 1 \\ 0, & \text{else} \end{cases}, \quad (4)$$

Fig. 1 visualizes the stable spikes decoupled by the  $\&$  operation, which reveal a clear feature skeleton with significantly less inconsistency compared to the original spike maps.

Furthermore, we define the stable spike firing rate,  $\tilde{\Phi} = \frac{1}{T-1} \sum_{t=0}^{T-2} \tilde{S}_t$ , to represent the aggregated feature of stable spikes over multiple timesteps.  $\tilde{\Phi}$  effectively represents the feature skeleton extracted by the SNN over multiple timesteps, so we align the variable spike map  $S$  to it to improve consistency and ignore spurious spike interference. To this end, we take the stable spike firing rate  $\tilde{\Phi}$  as an anchor point to guide the spike map  $S_t$ , and achieve the consistency constraint by backpropagation of the spike map consistency objective function.

During implementation, we use the mean squared error (MSE) function as the consistency guidance function and perform averaging on the original  $T$  spike feature maps to obtain the spike firing rate  $\Phi$ . Thus, the mathematical form

Table 1. Alternative consistency function.

Dataset	Vanilla	$\mathcal{L}_{spike}$			$\mathcal{L}_{noise}$		
		MSE	KL	Cosine	MSE	KL	Cosine
CIFAR10-DVS	72.9	<b>77.1</b>	76.2	75.6	76.1	<b>77.1</b>	76.0
DVS-Gesture	87.15	<b>94.44</b>	94.10	93.40	93.40	<b>94.44</b>	91.67

of spike map consistency alignment can be expressed as:

$$\begin{aligned} \mathcal{L}_{spike} &= MSE(\tilde{\Phi}, \Phi) \\ &= \frac{\sum_{i=1}^{C \times H \times W} (\frac{1}{T-1} \sum_{t=0}^{T-2} \tilde{S}_{i,t} - \frac{1}{T} \sum_{t=0}^{T-1} S_{i,t})^2}{C \times H \times W} \end{aligned} \quad (5)$$

During training, the gradient of  $\mathcal{L}_{spike}$  directly contributes to the stabilization of the spike firing rate, while preventing performance degradation due to excessive variance over multiple timesteps. Compared to the indirect adjustment of membrane potential and final output [6], the direct control of spike firing rate brings more significant consistency and superior discrimination performance. It is worth noting that our method is not limited to a specific consistency function. The results in Table 1 show that significant performance gains can also be achieved with KL divergence or cosine similarity, suggesting that our method promises to further unlock the performance of SNNs with an optimized consistency function implementation.

### 3.3. Amplitude-Aware Spike Noise for Perturbation Consistency

The feature diversity of neural networks can facilitate generalization under the premise of consistently preserving semantic information [11, 22]. Inspired by this, we expect to further increase the spike feature diversity to promote the generalization of SNNs. However, while ANNs can benefit from vanilla Gaussian noise [22], this does not work for SNNs due to the following two spike-specific character-

istics: (1) the inherent discrete property of binary spikes makes the addition of continuous Gaussian noise during training lead to training-inference precision mismatches; and (2) discrete spike firing rate is more sensitive to noise amplitude compared to floating-point numerical activation. Therefore, we propose amplitude-aware spike noise, which ensures that the SNN conveys discrete information through noise spikes during both training and inference, while the noise amplitude depends on the spike firing rate, ensuring that the perturbation promotes generalization without causing degradation.

A prerequisite for noise perturbation of features to facilitate generalization is the preservation of key semantic information [39]. Since the stable spike firing rate  $\tilde{\Phi}$  filters out differences across timesteps as a stable feature skeleton, we add noise to  $\tilde{\Phi}$  instead of directly perturbing the original features as in an ANN [22, 39]. The discrete value range of the stable spike firing rate  $\tilde{\Phi}$  decoupled within  $T$  timesteps is  $\{0, \frac{1}{T-1}, \dots, \frac{T-2}{T-1}, 1\}$ . To maintain the discrete property, we sample binary spike noise  $\varepsilon \in \{0, 1\}$  from the Bernoulli distribution with probability  $p$  and add it to the stable spike firing rate  $\tilde{\Phi}$  for perturbation. Specifically, the spike noise  $\varepsilon$  is obtained by randomly sampling the value  $p_{tmp}$  from  $[0, 1]$  and comparing it to the noise probability  $p$ . If  $p_{tmp}$  is less than or equal to  $p$ , a spike is generated. This is similar to value-dependent rate encoding of inputs, but requires only one random number generation and comparison, whereas input encoding requires multiple random samples to approximate the Poisson distribution [12, 20, 33]. After perturbation by the noise spike, the value range of the perturbed firing rate is  $\{0, \frac{1}{T-1}, \dots, \frac{T-2}{T-1}, 1, 1 + \frac{1}{T-1}, \dots, 1 + \frac{T-2}{T-1}, 2\}$ , which remains the discrete property.

On the one hand, if the spike feature value is small, excessive noise will disrupt the key semantics and cause performance degradation; on the other hand, a large spike feature value is insensitive to small noise perturbations, making it difficult to promote generalizability. To this end, we generate amplitude-aware spike noise by applying small perturbations to low firing rate elements and significant perturbations to higher firing rate elements, with the stable firing rate  $\tilde{\Phi}$  as the reference. For the implementation, we take the firing rate value of the corresponding position element in  $\tilde{\Phi}$  as the spike noise probability, i.e.,  $p_{c,i,j} = \tilde{\Phi}_{c,i,j}$ , where  $(c, i, j)$  denotes the position index. The amplitude-aware pulse noise can be expressed as:

$$\varepsilon_{c,i,j} = \begin{cases} 1, & \text{with probability } \tilde{\Phi}_{c,i,j} \\ 0, & \text{else} \end{cases}. \quad (6)$$

In this way, elements with a higher stable spike firing rate are more likely to be perturbed by a 1-value spike, and vice versa, elements with low firing rate are prevented from being excessively perturbed.

---

**Algorithm 1** The stable spike algorithm.

---

- 1: **Input:** training dataset  $\{x_i, y_i\}_{i=1}^B$ , timestep  $T$
  - 2: Initialization of parameters  $\theta$  in the SNN  $f(\cdot)$
  - 3: **for**  $t = 0$  **to**  $T - 1$  **do**
  - 4:   Forward propagation calculates the backbone spike map  $S_t = f(x)$
  - 5:   **if**  $t > 0$  **then**
  - 6:     Calculate the stable spike  $\tilde{S}_{t-1} = S_{t-1} \& S_t$
  - 7:     **end if**
  - 8:   Forward propagation produces the output  $O_t$
  - 9: **end for**
  - 10: Adding amplitude-aware spike noise  $\varepsilon$  to the stable spike firing rate  $\Phi_{noise} = \tilde{\Phi} + \varepsilon$
  - 11: Calculate the noise output  $O_{noise}$
  - 12: Calculate the dual consistency losses  $\leftarrow$  Eq. 9
  - 13: Backpropagation to optimize parameters  $\theta$
  - 14: **Output:** Consistency-optimized SNN
- 

After performing the noise perturbation on the stable spike firing rate to obtain  $\Phi_{noise} = \tilde{\Phi} + \varepsilon$ , we forward propagate the perturbed  $\Phi_{noise}$  to generate the final prediction  $O_{noise}$ . To allow the SNN to learn generalized representations, we align the probability distributions of the noisy prediction  $O_{noise}$  with the original clean prediction  $O$ . The temperature  $\alpha$  softening output logit is first used to obtain its probability distribution:

$$p_j = \frac{e^{O_j/\alpha}}{\sum_{k=1}^K e^{O_k/\alpha}}, p_{noise,j} = \frac{e^{O_{noise,j}/\alpha}}{\sum_{k=1}^K e^{O_{noise,k}/\alpha}}, \quad (7)$$

where  $j$  denotes the  $j$ -th class,  $K$  denotes a total of  $K$  classes, and temperature  $\alpha$  is set to 2. We use the KL divergence to promote consistency of the probability distribution after softening:

$$\mathcal{L}_{noise} = \alpha^2 KL(O || O_{noise}) = \alpha^2 \sum_{k=1}^K O_k \log\left(\frac{O_k}{O_{noise,k}}\right). \quad (8)$$

It is worth noting that the original SNN output  $O$  averaged over  $T$  timesteps is used as the final output; the noise prediction without temporal dimension is used directly as the final output. In addition, we compute stable spikes and perform consistency guidance only for the backbone features of the SNN, allowing additional forward propagation only past the classifier with negligible overhead.

During training, the spike map consistency loss (Eq. 5) and perturbation consistency loss (Eq. 8) are seamlessly combined with the cross-entropy loss of the classification task by balancing coefficients  $\beta$  and  $\gamma$ :

$$\mathcal{L}_{total} = \mathcal{L}_{CE} + \beta \mathcal{L}_{spike} + \gamma \mathcal{L}_{noise}. \quad (9)$$

The complete algorithm for training SNNs by stable spike is shown in Algorithm 1.

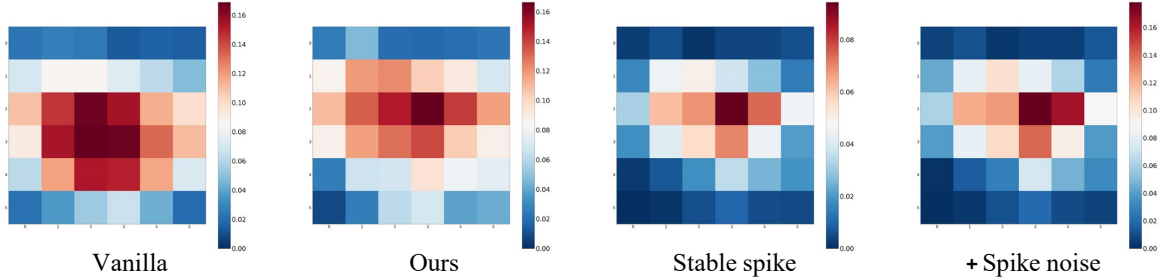


Figure 3. Comparison of spike firing rates. Our spike firing rate shows a clearer feature profile compared to the vanilla SNN by converging to the stable spike and reducing spike interference. Additionally, the proposed amplitude-aware spike noise preserves the key semantic features of stable spikes while increasing feature diversity, thereby improving generalization. To reflect the implementation, we visualize the SNN backbone output of VGG-9 with a spike map size of  $6 \times 6$ .

Table 2. Ablation results across different architectures.

Dataset	Method	VGG-9	ResNet-18	QKFormer
CIFAR10-DVS	Baseline	72.9	66.1	81.2
	+ $\mathcal{L}_{spike}$	75.2 $_{+2.4}$	69.7 $_{+3.6}$	82.5 $_{+1.3}$
	+ $\mathcal{L}_{noise}$	75.4 $_{+2.6}$	68.5 $_{+2.4}$	82.0 $_{+0.8}$
	+Both	<b>77.1<math>_{+4.2}</math></b>	<b>70.3<math>_{+4.2}</math></b>	<b>82.9<math>_{+1.7}</math></b>
DVS-Gesture	Baseline	87.15	81.59	93.75
	+ $\mathcal{L}_{spike}$	91.32 $_{+4.17}$	84.38 $_{+2.79}$	94.44 $_{+0.69}$
	+ $\mathcal{L}_{noise}$	94.09 $_{+6.94}$	83.68 $_{+2.09}$	94.79 $_{+1.04}$
	+Both	<b>94.44<math>_{+7.29}</math></b>	<b>85.42<math>_{+3.83}</math></b>	<b>95.49<math>_{+1.74}</math></b>

## 4. Experiments

We focus on neuromorphic benchmarks CIFAR10-DVS [21], DVS-Gesture [1], and N-Caltech101 [28], while also conducting validation on static CIFAR10/100 and ImageNet using VGG, ResNet, and Transformer-style architectures to demonstrate the effectiveness and generalizability of our method. For VGG-9 and ResNet-18, we use the same training strategy as MPS [6]; for QKFormer, we also follow its original strategy [54]. If not specified, the consistency loss balance coefficients  $\beta$  and  $\gamma$  are set to 1.0, and the timestep is 4 to reflect the low-latency performance of the SNN. The detailed experimental setup can be found in the **Supplementary Material**.

### 4.1. Ablation Study

To demonstrate the effectiveness and versatility of the proposed method, we performed ablation studies with three architectures on CIFAR10-DVS and DVS-Gesture, and the results are shown in Table 2. The results show that the proposed method consistently delivers performance gains for different SNN architectures, in particular up to 7.29% for DVS-Gesture recognition with VGG-9. When applied to the QKFormer [54] with SOTA performance, the performance is further improved, demonstrating the superior generalizability of our method.

In addition, we examine the effects of two key components of amplitude-aware spike noise: amplitude adaptation and spike noise. We perturbed the stable spike firing rate with a fixed noise spike probability  $p$  and continuous Gaussian noise with mean value 0, respectively, and

Table 3. The effectiveness of amplitude adaption and discrete spike noise.  $p$  is the fixed noise spike probability and  $std$  is the standard deviation of the continuous Gaussian noise.

Dataset	Ablation	Acc. (%)	Dataset	Ablation	Acc. (%)
CIFAR10-DVS	$p = 0.4$	74.8	DVS-Gesture	$p = 0.4$	87.15
	$p = 0.5$	75.1		$p = 0.5$	88.89
	$p = 0.6$	75.5		$p = 0.6$	86.81
	$std = 0.1$	74.9	$std = 0.1$	88.19	
	$std = 0.5$	75.3	$std = 0.5$	91.67	
	$std = 1.0$	74.5	$std = 1.0$	89.93	
	Ours	<b>77.1</b>	Ours	<b>94.44</b>	

Table 4. Comparison (%) of AND, OR, and XOR bit operations.

Dataset	AND	OR	XOR
CIFAR10-DVS	<b>77.1</b>	68.9	74.5
DVS-Gesture	<b>94.44</b>	88.54	89.58

the results are shown in Table 3. The results show that using the fixed noise spike probability whose amplitude is uncontrollable significantly degrades the performance of the proposed method; replacing the discrete spike noise with continuous Gaussian noise also leads to degraded performance. In particular, when the fixed noise probability is excessively high, leading to overly strong perturbations ( $p = 0.75$ ), the model fails to converge. In contrast, the proposed amplitude-aware spike noise considers the discrete, noise-sensitive properties of SNNs and demonstrates superior performance.

Table 4 compares the performance of AND and other bit operations (OR and XOR). The AND operation consistently retrieves (1, 1) spike pairs, whereas the OR and XOR operations retrieve the  $\{(1, 0), (0, 1), (1, 1)\}$  and  $\{(0, 1), (1, 0)\}$  patterns, respectively. The results show that the AND operation achieves optimal performance, which aligns with our insights on consistency. Notably, the OR operation caused significant degradation due to the simultaneous retrieval of consistent/inconsistent spike patterns triggering confusion.

To investigate the influence of  $\beta$  and  $\gamma$  on the performance, we conducted experiments on DVS-Gesture in the range  $\{0.1, 0.25, 0.5, 0.75, 1.0, 1.25, 1.5, 1.75, 2.0\}$ . The results in Fig. 4 show that these coefficients affect the per-

Table 5. Comparative results (%) on neuromorphic datasets. † denotes knowledge transfer from static data.

	Method	Architecture	$T \downarrow$	Acc. (%) $\uparrow$	
CIFAR10-DVS	STAA-SNN <sup>CVPR'25</sup> [52]	VGG-13	16	82.1	
	SLT <sup>AAAI'24</sup> [2]	VGGSNN	10	81.46	
	DeepTAGE <sup>ICLR'25</sup> [25]	VGG-11	10	81.23	
	EnOF-SNN <sup>NeurIPS'24</sup> [14]	ResNet20	10	80.5	
	BKDSNN <sup>ECCV'24</sup> [43]	Wide-7B-Net	8	72.2	
	SSNN <sup>AAAI'24</sup> [5]	VGG-9	5	73.63	
	MPS <sup>ICLR'25</sup> [6]	VGG-9	5	76.77	
		VGGSNN	4	83.2	
	<b>Ours</b>	VGG-9	4	<b>77.1</b>	
		VGGSNN	4	<b>83.7</b>	
	SNN-ViT <sup>ICLR'25</sup> [38]	SNN-ViT	16	82.3	
	SWformer <sup>ECCV'24</sup> [10]	SWformer	10	82.9	
	SEMM <sup>NeurIPS'24</sup> [55]	Spikingformer	10	80.7	
	SpikingResformer <sup>CVPR'24</sup> [37]	SpikingResformer	10	81.5	
	MPS <sup>ICLR'25</sup> [6]	SpikingResformer	5	80.6	
QKFormer <sup>NeurIPS'24</sup> [54]	QKFormer	4	81.2		
<b>Ours</b>	QKFormer	4	<b>82.9</b>		
MPS <sup>ICLR'25</sup> [6]	VGG-9	5	93.23		
SSNN <sup>AAAI'24</sup> [5]	VGG-9	5	90.74		
CLIF <sup>ICML'24</sup> [18]	VGG-9	4	89.58		
TAB <sup>ICLR'24</sup> [19]	VGG-9	4	87.50		
SLT <sup>AAAI'24</sup> [2]	VGG-9	4	88.19		
<b>Ours</b>	VGG-9	4	<b>94.44</b>		
DVS-Gesture	QKFormer <sup>NeurIPS'24</sup> [54]	QKFormer	16	98.60	
	SpikingResformer <sup>CVPR'24</sup> [37]	SpikingResformer	16	98.60	
	SEMM <sup>NeurIPS'24</sup> [55]	Spikingformer	10	96.88	
	MPS <sup>ICLR'25</sup> [6]	SpikingResformer	5	94.44	
	QKFormer <sup>NeurIPS'24</sup> [54]	QKFormer	4	93.75	
	<b>Ours</b>	QKFormer	4	<b>95.49</b>	
			16	<b>98.61</b>	
	N-Caltech101	TCJA-TET-SNN <sup>TNNLS'24</sup> [56]	CombinedSNN	14	82.50
		SWformer <sup>ECCV'24</sup> [10]	SWformer	10	88.45
		IMP+TET-S <sup>NeurIPS'24</sup> [35]	VGGSNN	10	85.01
TKS <sup>IEEE TAI'24</sup> [8]		VGGSNN	10	84.10	
EventMix <sup>Inf.Sci.'23</sup> [34]		ResNet-18	10	79.47	
TIM <sup>IJCAI'24</sup> [36]		Spikformer	10	79.00	
NDA <sup>ECCV'22</sup> [23]		VGG-11	10	78.20	
Knowledge-Transfer <sup>AAAI'24</sup> [16]		VGGSNN	10	93.18†	
SSNN <sup>AAAI'24</sup> [5]		VGG-9	5	77.97	
		VGG-9	5	82.71	
MPS <sup>ICLR'25</sup> [6]		VGGSNN	10	93.68†	
<b>Ours</b>		VGG-9	4	<b>83.92</b>	
		VGGSNN	10	<b>94.25†</b>	

formance to a certain extent, where the lowest accuracy is 92.01%, while the highest accuracy reaches 95.14%. It is worth noting that although the performance fluctuates, the lower bound of our method still far exceeds the performance of the vanilla SNN (87.15%). This suggests that our method can be plug-and-play to improve performance and offers higher potential after adjusting the balancing coefficients.

## 4.2. Comparison with Other Methods

**Neuromorphic Benchmark.** Table 5 shows the comparative results on neuromorphic benchmarks. Without any data augmentation, our VGG-9 achieved a competitive accuracy of 77.1% on CIFAR10-DVS with only 4 timesteps. Using

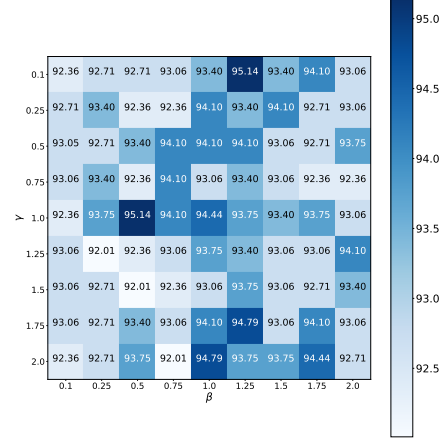


Figure 4. Performance (%) of different balance coefficients  $\beta$  and  $\gamma$  on DVS-Gesture.

Table 6. Comparative results with other methods on ImageNet.

Method	Architecture	$T$	Acc.(%)
RateBP [49] <sup>NeurIPS'24</sup>	ResNet-34	4	70.01
TAB [19] <sup>ICLR'24</sup>	ResNet34	4	67.78
Shortcut [13] <sup>NeurIPS'24</sup>	ResNet34	4	68.14
FSTA-SNN [50] <sup>AAAI'25</sup>	ResNet34	4	70.23
STAA-SNN [52] <sup>CVPR'25</sup>	ResNet34	4	70.40
IMP+LTS [35] <sup>ICLR'25</sup>	ResNet34	4	68.90
SSCL [53] <sup>AAAI'24</sup>	ResNet34	4	66.78
EnOF [14] <sup>NeurIPS'24</sup>	ResNet34	4	67.40
MPS [6] <sup>ICLR'25</sup>	ResNet-34	4	69.03
Strong2Weak [7] <sup>NeurIPS'25</sup>	ResNet-34	4	70.53
Weak2Strong [7] <sup>NeurIPS'25</sup>	ResNet-34	4	69.87
<b>Ours</b>	ResNet-34	4	<b>70.59</b>

standard data augmentation and the VGGSNN architecture, recognition accuracy reaches 83.7%. On DVS-Gesture and N-Caltech101, our method also achieves significant performance advantages at low latency. In particular, our method can be used in conjunction with Knowledge-Transfer [16] to achieve 94.25% accuracy on N-Caltech101 at 10 timesteps, exceeding all other methods.

**Static Dataset.** Table 6 presents the comparative results on ImageNet. We achieved an accuracy of 70.59% using ResNet-34 with four timesteps, surpassing other comparative methods. On CIFAR10 and CIFAR100, we achieved accuracies of 96.73% and 82.29%, respectively, once again outperforming other methods. See **Supplementary Material** for details.

## 4.3. Loss Landscape Visualization

To demonstrate the effectiveness of the proposed method from an optimization standpoint, Fig. 5 visually compares the loss landscapes of the vanilla SNN and the proposed method. In Fig. 5(a)(c), the loss distribution of the vanilla SNN is dispersed and irregular, especially the upper-right and the center regions differ significantly. Additionally, local minima interfere with optimization, causing the model

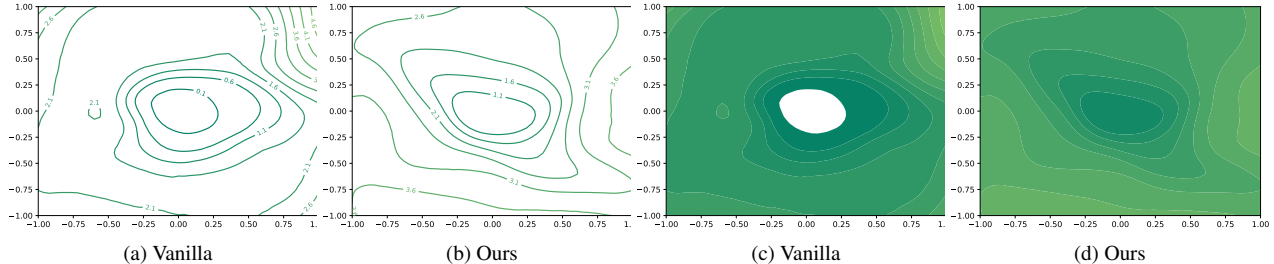


Figure 5. Visualization of loss landscapes. (a) (c) The loss landscape of the vanilla SNN exhibits multiple local minima and saddle points. This complexity makes optimization susceptible to falling into local optima. (b) (d) Our method has a smoother and more centralized loss landscape with a clear global minimum, which makes optimization stable and convergent.

Table 7. Scalable performance across timesteps. Our method improves performance consistently from ultra-low to high latencies.

Dataset	$T = 2$		$T = 4$		$T = 6$		$T = 8$		$T = 10$	
	Vanilla	Ours	Vanilla	Ours	Vanilla	Ours	Vanilla	Ours	Vanilla	Ours
CIFAR10-DVS	72.6	<b>74.6</b> <sub>+2.0</sub>	72.9	<b>77.1</b> <sub>+4.2</sub>	73.7	<b>77.5</b> <sub>+3.8</sub>	75.2	<b>77.8</b> <sub>+2.6</sub>	75.5	<b>78.2</b> <sub>+2.7</sub>
DVS-Gesture	83.68	<b>92.01</b> <sub>+8.33</sub>	87.15	<b>94.44</b> <sub>+7.29</sub>	88.19	<b>94.10</b> <sub>+5.91</sub>	90.97	<b>95.49</b> <sub>+4.52</sub>	92.01	<b>95.49</b> <sub>+3.48</sub>

Table 8. Comparison of spike firing rate (%) and power consumption ( $\times 10^6 pJ$ ) on CIFAR10-DVS with VGG-9.

Layer $\rightarrow$	1	2	3	4	5	6	7	8	Power $\downarrow$
Vanilla	<b>9.24</b>	4.26	3.38	3.12	2.17	1.45	1.20	7.63	189.83
<b>Ours</b>	10.14	<b>3.61</b>	<b>3.20</b>	<b>2.88</b>	<b>1.70</b>	<b>1.25</b>	<b>1.10</b>	<b>9.81</b>	<b>181.02</b>

to be highly susceptible to falling into local optimal solutions. In contrast, the loss landscape of our method (Fig. 5(b)(d)) is much smoother overall, without sharp variance despite the presence of spike noise perturbation during training. Consequently, our method is capable of converging to the global optimal solution with enhanced stability and efficiency, thereby facilitating generalization.

#### 4.4. Scalability with Timesteps

Table 7 shows the performance variation of the proposed method with different timesteps. We vary the timestep from the commonly used high latency ( $T = 10$ ) to the ultra-low latency ( $T = 2$ ). The results show that our method yields consistent performance gains that generalize to a wide range of latencies. In particular, the accuracy on DVS-Gesture is improved by 8.33% at  $T = 2$ , which significantly contributes to the development of ultra-low latency SNNs.

#### 4.5. Spike Firing Rate and Power Consumption

To investigate the influence of our method on spike firing rate and power consumption, we present the comparative results with the vanilla SNN in Table 8. The results show that our method achieves lower firing rates and lower overall power consumption across all layers except the first. This indicates that our method not only improves the performance of SNNs, but also slightly reduces their power consumption during deployment.

#### 4.6. Compatibility with Other Methods

Our method is a plug-and-play SNN enhancement algorithm that requires no modification to the neuron model or

Table 9. Our method can be seamlessly integrated with other methods and exhibits superior generalizability.

Dataset	Type	Method	Acc. (%)	+ Ours
CIFAR10-DVS	Spiking neuron	CLIF [18]	74.3	<b>76.2</b> <sub>+1.9</sub>
	BN Layer	TAB [19]	73.1	<b>75.4</b> <sub>+2.3</sub>
	Training	SLT [2]	74.1	<b>75.9</b> <sub>+1.8</sub>
DVS-Gesture	Spiking neuron	CLIF [18]	89.58	<b>95.83</b> <sub>+6.25</sub>
	BN Layer	TAB [19]	87.50	<b>92.36</b> <sub>+4.86</sub>
	Training	SLT [2]	88.19	<b>90.97</b> <sub>+2.78</sub>

architecture. To further validate the compatibility, we combine our method with other SNN methods, including the improved neuron model CLIF [18], the SNN-oriented BN layer TAB [19], and the efficient training algorithm SLT [2]. The results in Table 9 show that our method consistently improves the performance of these methods, suggesting that our method has the potential to efficiently facilitate the performance of more SNN methods in the future.

## 5. Conclusion

In this paper, we decouple the stable spike skeleton via the “AND” bit operation, and motivate the spike maps to converge towards it for consistency. Furthermore, we inject amplitude-aware spike noise to facilitate spike feature diversity while preserving key semantics, encouraging the SNN to generate perturbation-consistent predictions for generalization. Our method is neuron-architecture agnostic and can therefore be used to boost the performance of other SNN methods as a plug-and-play solution. Extensive experiments demonstrate the effectiveness and performance advantages of our method. We expect this work to inspire advancements in ultra-low-latency, high-performance SNNs.

## Acknowledgments

This work was supported by the National Natural Science Foundation of China under Grant No. 62276054.

## References

- [1] Arnon Amir et al. A low power, fully event-based gesture recognition system. In *2017 IEEE Conference on Computer Vision and Pattern Recognition (CVPR)*, pages 7388–7397, 2017. 6, 12
- [2] Srinivas Anumasa, Bhaskar Mukhoty, Velibor Bojkovic, Giulia De Masi, Huan Xiong, and Bin Gu. Enhancing training of spiking neural network with stochastic latency. In *Proceedings of the AAAI Conference on Artificial Intelligence*, pages 10900–10908, 2024. 2, 3, 7, 8, 12, 14
- [3] Ekin D Cubuk, Barret Zoph, Dandelion Mane, Vijay Vasudevan, and Quoc V Le. Autoaugment: Learning augmentation strategies from data. In *Proceedings of the IEEE/CVF conference on computer vision and pattern recognition*, pages 113–123, 2019. 12
- [4] Terrance DeVries and Graham W Taylor. Improved regularization of convolutional neural networks with cutout. *arXiv preprint arXiv:1708.04552*, 2017. 12
- [5] Yongqi Ding, Lin Zuo, Mengmeng Jing, Pei He, and Yongjun Xiao. Shrinking your timestep: Towards low-latency neuromorphic object recognition with spiking neural networks. In *Proceedings of the AAAI Conference on Artificial Intelligence*, pages 11811–11819, 2024. 1, 3, 7
- [6] Yongqi Ding, Lin Zuo, Mengmeng Jing, Pei He, and Hanpu Deng. Rethinking spiking neural networks from an ensemble learning perspective. In *The Thirteenth International Conference on Learning Representations*, 2025. 1, 2, 3, 4, 6, 7, 12, 13
- [7] Yongqi Ding, Lin Zuo, Mengmeng Jing, Kunshan Yang, Pei He, and Tonglan Xie. Synergy between the strong and the weak: Spiking neural networks are inherently self-distillers. In *The Thirty-ninth Annual Conference on Neural Information Processing Systems*, 2025. 3, 7, 14
- [8] Yiting Dong, Dongcheng Zhao, and Yi Zeng. Temporal knowledge sharing enable spiking neural network learning from past and future. *IEEE Transactions on Artificial Intelligence*, 5(7):3524–3534, 2024. 3, 7
- [9] Wei Fang, Zhaofei Yu, Zhaokun Zhou, Ding Chen, Yanqi Chen, Zhengyu Ma, Timothée Masquelier, and Yonghong Tian. Parallel spiking neurons with high efficiency and ability to learn long-term dependencies. *Advances in Neural Information Processing Systems*, 36, 2023. 2
- [10] Yuetong Fang, Ziqing Wang, Lingfeng Zhang, Jiahang Cao, Honglei Chen, and Renjing Xu. Spiking wavelet transformer. In *Computer Vision – ECCV 2024*, pages 19–37, Cham, 2025. Springer Nature Switzerland. 3, 7
- [11] Zhi Gao, Yuwei Wu, Yunde Jia, and Mehrtash Harandi. Hyperbolic feature augmentation via distribution estimation and infinite sampling on manifolds. In *Advances in Neural Information Processing Systems*, 2022. 2, 4
- [12] Wenzhe Guo, Mohammed E Fouda, Ahmed M Eltawil, and Khaled Nabil Salama. Neural coding in spiking neural networks: A comparative study for robust neuromorphic systems. *Frontiers in Neuroscience*, 15:638474, 2021. 5
- [13] Yufei Guo, Yuanpei Chen, Zecheng Hao, Weihang Peng, Zhou Jie, Yuhan Zhang, Xiaode Liu, and Zhe Ma. Take a shortcut back: Mitigating the gradient vanishing for training spiking neural networks. In *The Thirty-eighth Annual Conference on Neural Information Processing Systems*, 2024. 7
- [14] Yufei Guo, Weihang Peng, Xiaode Liu, Yuanpei Chen, Yuhan Zhang, Xin Tong, Zhou Jie, and Zhe Ma. EnOF-SNN: Training accurate spiking neural networks via enhancing the output feature. In *The Thirty-eighth Annual Conference on Neural Information Processing Systems*, 2024. 3, 7
- [15] Yufei Guo, Yuhan Zhang, Zhou Jie, Xiaode Liu, Xin Tong, Yuanpei Chen, Weihang Peng, and Zhe Ma. Reverb-SNN: Reversing bit of the weight and activation for spiking neural networks. In *Forty-second International Conference on Machine Learning*, 2025. 14
- [16] Xiang He, Dongcheng Zhao, Yang Li, Guobin Shen, Qingqun Kong, and Yi Zeng. An efficient knowledge transfer strategy for spiking neural networks from static to event domain. In *Proceedings of the AAAI Conference on Artificial Intelligence*, pages 512–520, 2024. 3, 7, 12
- [17] S. G. Hu, G. C. Qiao, X. K. Liu, Y. H. Liu, C. M. Zhang, Yue Zuo, Pujun Zhou, Y. A. Liu, Ning Ning, Qi Yu, and Yang Liu. A co-designed neuromorphic chip with compact (17.9k f2) and weak neuron number-dependent neuron/synapse modules. *IEEE Transactions on Biomedical Circuits and Systems*, 16(6):1250–1260, 2022. 1
- [18] Yulong Huang, Xiaopeng LIN, Hongwei Ren, Haotian FU, Yue Zhou, Zunchang LIU, biao pan, and Bojun Cheng. CLIF: Complementary leaky integrate-and-fire neuron for spiking neural networks. In *Forty-first International Conference on Machine Learning*, 2024. 2, 7, 8, 12
- [19] Haiyan Jiang, Vincent Zoonekynd, Giulia De Masi, Bin Gu, and Huan Xiong. TAB: Temporal accumulated batch normalization in spiking neural networks. In *The Twelfth International Conference on Learning Representations*, 2024. 7, 8, 12
- [20] Youngeun Kim, Hyoungeob Park, Abhishek Moitra, Abhiroop Bhattacharjee, Yeshwanth Venkatesha, and Priyadarshini Panda. Rate coding or direct coding: Which one is better for accurate, robust, and energy-efficient spiking neural networks? In *ICASSP 2022 - 2022 IEEE International Conference on Acoustics, Speech and Signal Processing (ICASSP)*, pages 71–75, 2022. 5
- [21] Hongmin Li, Hanchao Liu, Xiangyang Ji, Guoqi Li, and Luping Shi. Cifar10-dvs: An event-stream dataset for object classification. *Frontiers in Neuroscience*, 11, 2017. 6, 12
- [22] Pan Li, Da Li, Wei Li, Shaogang Gong, Yanwei Fu, and Timothy M. Hospedales. A simple feature augmentation for domain generalization. In *Proceedings of the IEEE/CVF International Conference on Computer Vision (ICCV)*, pages 8886–8895, 2021. 2, 4, 5
- [23] Yuhang Li, Youngeun Kim, Hyoungeob Park, Tamar Geller, and Priyadarshini Panda. Neuromorphic data augmentation for training spiking neural networks. In *European Conference on Computer Vision*, pages 631–649. Springer, 2022. 3, 7
- [24] Shuang Lian, Jiangrong Shen, Qianhui Liu, Ziming Wang, Rui Yan, and Huajin Tang. Learnable surrogate gradient for direct training spiking neural networks. In *IJCAI*, pages 3002–3010, 2023. 14

- [25] Wei Liu, Li Yang, Mingxuan Zhao, Shuxun Wang, Jin Gao, Wenjuan Li, Bing Li, and Weiming Hu. DeepTAGE: Deep temporal-aligned gradient enhancement for optimizing spiking neural networks. In *The Thirteenth International Conference on Learning Representations*, 2025. 3, 7, 14
- [26] De Ma, Xiaofei Jin, Shichun Sun, Yitao Li, Xundong Wu, Youneng Hu, Fangchao Yang, Huajin Tang, Xiaolei Zhu, Peng Lin, and Gang Pan. Darwin3: a large-scale neuromorphic chip with a novel isa and on-chip learning. *National Science Review*, 11(5):nwae102, 2024. 1
- [27] Wolfgang Maass. Networks of spiking neurons: The third generation of neural network models. *Neural Networks*, 10(9):1659–1671, 1997. 1
- [28] Garrick Orchard, Ajinkya Jayawant, Gregory K. Cohen, and Nitish Thakor. Converting static image datasets to spiking neuromorphic datasets using saccades. *Frontiers in Neuroscience*, 9, 2015. 6, 12
- [29] Jisung Park, Roknoddin Azizi, Geraldo F. Oliveira, Mohammad Sadrosadati, Rakesh Nadig, David Novo, Juan Gómez-Luna, Myungsuk Kim, and Onur Mutlu. Flash-cosmos: In-flash bulk bitwise operations using inherent computation capability of nand flash memory. In *2022 55th IEEE/ACM International Symposium on Microarchitecture (MICRO)*, pages 937–955, 2022. 1
- [30] Wachirawit Ponghiran and Kaushik Roy. Spiking neural networks with improved inherent recurrence dynamics for sequential learning. In *Proceedings of the AAAI Conference on Artificial Intelligence*, pages 8001–8008, 2022. 2
- [31] Haonan Qiu, Zeyin Song, Yanqi Chen, Munan Ning, Wei Fang, Tao Sun, Zhengyu Ma, Li Yuan, and Yonghong Tian. Temporal contrastive learning for spiking neural networks. In *Artificial Neural Networks and Machine Learning – ICANN 2024*, pages 422–436, 2024. 3
- [32] Kaushik Roy, Akhilesh Jaiswal, and Priyadarshini Panda. Towards spike-based machine intelligence with neuromorphic computing. *Nature*, 575(7784):607–617, 2019. 1, 2
- [33] Saima Sharmin, Nitin Rathi, Priyadarshini Panda, and Kaushik Roy. Inherent adversarial robustness of deep spiking neural networks: Effects of discrete input encoding and non-linear activations. In *Computer Vision – ECCV 2020*, pages 399–414, Cham, 2020. Springer International Publishing. 5
- [34] Guobin Shen, Dongcheng Zhao, and Yi Zeng. Eventmix: An efficient data augmentation strategy for event-based learning. *Information Sciences*, 644:119170, 2023. 3, 7
- [35] Hangchi Shen, Qian Zheng, Huamin Wang, and Gang Pan. Rethinking the membrane dynamics and optimization objectives of spiking neural networks. In *The Thirty-eighth Annual Conference on Neural Information Processing Systems*, 2024. 7
- [36] Sicheng Shen, Dongcheng Zhao, Guobin Shen, and Yi Zeng. Tim: An efficient temporal interaction module for spiking transformer, 2024. 7
- [37] Xinyu Shi, Zecheng Hao, and Zhaofei Yu. Spikingresformer: Bridging resnet and vision transformer in spiking neural networks. In *Proceedings of the IEEE/CVF Conference on Computer Vision and Pattern Recognition (CVPR)*, pages 5610–5619, 2024. 7
- [38] Shuai Wang, Malu Zhang, Dehao Zhang, Ammar Belatreche, Yichen Xiao, Yu Liang, Yimeng Shan, Qian Sun, Enqi Zhang, and Yang Yang. Spiking vision transformer with saccadic attention. In *The Thirteenth International Conference on Learning Representations*, 2025. 2, 7, 14
- [39] Yulin Wang, Xuran Pan, Shiji Song, Hong Zhang, Gao Huang, and Cheng Wu. Implicit semantic data augmentation for deep networks. In *Advances in Neural Information Processing Systems*. Curran Associates, Inc., 2019. 5
- [40] Jibin Wu, Chenglin Xu, Xiao Han, Daquan Zhou, Malu Zhang, Haizhou Li, and Kay Chen Tan. Progressive tandem learning for pattern recognition with deep spiking neural networks. *IEEE Transactions on Pattern Analysis and Machine Intelligence*, 44(11):7824–7840, 2022. 1, 2
- [41] Yujie Wu, Lei Deng, Guoqi Li, Jun Zhu, and Luping Shi. Spatio-temporal backpropagation for training high-performance spiking neural networks. *Frontiers in neuroscience*, 12:331, 2018. 3
- [42] Qi Xu, Yaxin Li, Jiangrong Shen, Jian K. Liu, Huajin Tang, and Gang Pan. Constructing deep spiking neural networks from artificial neural networks with knowledge distillation. In *Proceedings of the IEEE/CVF Conference on Computer Vision and Pattern Recognition (CVPR)*, pages 7886–7895, 2023. 3, 14
- [43] Zekai Xu, Kang You, Qinghai Guo, Xiang Wang, and Zhezhi He. Bkdsnn: Enhancing the performance of learning-based spiking neural networks training with blurred knowledge distillation. In *Computer Vision – ECCV 2024*, pages 106–123, Cham, 2024. 3, 7
- [44] Bonan Yan, Jeng-Long Hsu, Pang-Cheng Yu, Chia-Chi Lee, Yaojun Zhang, Wenshuo Yue, Guoqiang Mei, Yuchao Yang, Yue Yang, Hai Li, Yiran Chen, and Ru Huang. A 1.041-mb/mm<sup>2</sup> 27.38-tops/w signed-int8 dynamic-logic-based adc-less sram compute-in-memory macro in 28nm with reconfigurable bitwise operation for ai and embedded applications. In *2022 IEEE International Solid-State Circuits Conference (ISSCC)*, pages 188–190, 2022. 1
- [45] Jiaqi Yan, Changping Wang, De Ma, Huajin Tang, Qian Zheng, and Gang Pan. Training high performance spiking neural network by temporal model calibration. In *Forty-second International Conference on Machine Learning*, 2025. 14
- [46] Zheyu Yang, Taoyi Wang, Yihan Lin, Yuguo Chen, Hui Zeng, Jing Pei, Jiazheng Wang, Xue Liu, Yichun Zhou, Jianqiang Zhang, et al. A vision chip with complementary pathways for open-world sensing. *Nature*, 629(8014):1027–1033, 2024. 1, 2
- [47] Man Yao, JiaKui Hu, Zhaokun Zhou, Li Yuan, Yonghong Tian, Bo Xu, and Guoqi Li. Spike-driven transformer. In *Advances in Neural Information Processing Systems*, pages 64043–64058. Curran Associates, Inc., 2023. 2
- [48] Man Yao, Ole Richter, Guangshe Zhao, Ning Qiao, Yannan Xing, Dingheng Wang, Tianxiang Hu, Wei Fang, Tugba Demirci, Michele De Marchi, et al. Spike-based dynamic computing with asynchronous sensing-computing neuromorphic chip. *Nature Communications*, 15(1):4464, 2024. 1, 2, 3

- [49] Chengting Yu, Lei Liu, Gaoang Wang, Erping Li, and Aili Wang. Advancing training efficiency of deep spiking neural networks through rate-based backpropagation. In *The Thirty-eighth Annual Conference on Neural Information Processing Systems*, 2024. 7, 14
- [50] Kairong Yu, Tianqing Zhang, Hongwei Wang, and Qi Xu. Fsta-snn: Frequency-based spatial-temporal attention module for spiking neural networks. In *Proceedings of the AAAI Conference on Artificial Intelligence*, pages 22227–22235, 2025. 7
- [51] Kairong Yu, Tianqing Zhang, Qi Xu, Gang Pan, and Hongwei Wang. TS-SNN: Temporal shift module for spiking neural networks. In *Forty-second International Conference on Machine Learning*, 2025. 14
- [52] Tianqing Zhang, Kairong Yu, Xian Zhong, Hongwei Wang, Qi Xu, and Qiang Zhang. Staa-snn: Spatial-temporal attention aggregator for spiking neural networks. In *Proceedings of the IEEE/CVF Conference on Computer Vision and Pattern Recognition (CVPR)*, pages 13959–13969, 2025. 3, 7, 14
- [53] Yuhan Zhang, Xiaode Liu, Yuanpei Chen, Weihang Peng, Yufei Guo, Xuhui Huang, and Zhe Ma. Enhancing representation of spiking neural networks via similarity-sensitive contrastive learning. In *Proceedings of the AAAI Conference on Artificial Intelligence*, pages 16926–16934, 2024. 3, 7
- [54] Chenlin Zhou, Han Zhang, Zhaokun Zhou, Liutao Yu, Liwei Huang, Xiaopeng Fan, Li Yuan, Zhengyu Ma, Huihui Zhou, and Yonghong Tian. QKFormer: Hierarchical spiking transformer using q-k attention. In *The Thirty-eighth Annual Conference on Neural Information Processing Systems*, 2024. 2, 6, 7, 12, 14
- [55] Zhaokun Zhou, Yijie Lu, Yanhao Jia, Kaiwei Che, Jun Niu, Liwei Huang, Xinyu Shi, Yuesheng Zhu, Guoqi Li, Zhaofei Yu, and Li Yuan. Spiking transformer with experts mixture. In *The Thirty-eighth Annual Conference on Neural Information Processing Systems*, 2024. 7
- [56] Rui-Jie Zhu, Malu Zhang, Qihang Zhao, Haoyu Deng, Yule Duan, and Liang-Jian Deng. Tcja-snn: Temporal-channel joint attention for spiking neural networks. *IEEE Transactions on Neural Networks and Learning Systems*, pages 1–14, 2024. 7
- [57] Lin Zuo, Yongqi Ding, Mengmeng Jing, Kunshan Yang, and Yunqian Yu. Self-distillation learning based on temporal-spatial consistency for spiking neural networks. *arXiv preprint arXiv:2406.07862*, 2024. 3

## Description of the Supplementary Material

This supplementary material contains four sections:

Section A interprets the effectiveness of the AND operation from the perspective of mutual information.

Section B details the experimental setup, including the dataset and training strategy.

Section C presents additional experimental results, including further comparative experiments and extensions of our method.

Section D provides an overhead analysis showing that our method requires only negligible training overhead and leaves inference completely unaffected.

Section E provides supplementary visualizations demonstrating that the AND operation consistently extracts stable pulse skeletons.

## A. Interpreting the AND Operation from the Perspective of Mutual Information

The AND operation extracts the mutual information between adjacent timesteps. The  $(1, 1)$  pair represents the consensus feature between two consecutive timesteps, which eliminates transient noise. According to the information bottleneck principle, the convergence of spike maps toward stable spikes maximizes mutual information in order to identify the minimal sufficient representation. In contrast, the XOR and XOR operations are inferior to the AND operation and may even exhibit degradation due to interference from  $(0, 0)$  and  $(0, 1)$ .

## B. Experimental Details

### B.1. Neuromorphic Datasets.

We conducted experiments on three neuromorphic object recognition benchmark datasets: CIFAR10-DVS [21], DVS-Gesture [1], and N-Caltech101 [28]. The CIFAR10-DVS [21] dataset contains a total of 10,000 samples from ten categories. The DVS-Gesture [1] dataset contains neuromorphic data for 11 hand gestures with 1176 training samples and 288 test samples. The spatial resolution of each sample in CIFAR10-DVS and DVS-Gesture is  $128 \times 128$ , which we downsampled to  $48 \times 48$  and input to SNN, the standard input size for the community [6, 54]. The N-Caltech101 [28] dataset contains 8,109 samples, categorized into 101 categories, with an original resolution of  $180 \times 240$ . We also downsampled the samples in N-Caltech101 to  $48 \times 48$ .

We conducted our experiments on an Ubuntu 20.04.5 operating system with an NVIDIA 4090 GPU. To validate the versatility of the proposed method, we conducted experiments using various architectures, including VGG-9, ResNet-18, VGGSNN, and QKFormer. For VGG-9 and ResNet-18, we use the same training strategy as in [6]. The model was trained for 100 epochs using a stochastic gradient descent optimizer. The initial learning rate was set to 0.1, and it was scaled down tenfold every 30 epochs. The batch size is 64, and the weight decay is  $1e-3$ . In particular, for VGG-9 and ResNet-18, we do not use any data augmentation during training. The firing threshold of the spiking neuron was set to 1.0, and the membrane potential time constant was set to 2.0. In the training of the SNN, the rectangular surrogate gradient function is employed for backpropagation, consistent with [6]. Table 10 shows the VGG-9 and ResNet-18 architectures.

When using VGGSNN for recognizing CIFAR10-DVS, we used random cropping and horizontal flipping as data augmentation. When using the VGGSNN architecture on the N-Caltech101 dataset, we incorporate the knowledge transfer strategy [16] and employ the same training strategy as in [16]. Similarly, when using the QKFormer architec-

ture, we follow the training strategy outlined in the original paper [54] to ensure the fairness of the experiments. We set the balancing coefficients  $\beta$  and  $\gamma$  to 1.0 by default, and the experiments in Section 4.1 demonstrate the influence of these coefficients on performance. However, when we use VGGSNN to recognize the N-Caltech101 dataset and incorporate knowledge transfer, the magnitude of our loss does not match the original transfer loss. At this point, we set the balancing coefficients to  $1e-3$ .

### B.2. Static Datasets.

For static images, we conducted experiments on the CIFAR10 and CIFAR100 datasets. Both the CIFAR-10 and CIFAR-100 datasets contain 60,000  $32 \times 32$  images, 50,000 of which are in the training set and 10,000 of which are in the test set. We normalized the CIFAR10 and CIFAR100 samples to a zero mean and unit variance. Then, we applied the standard data augmentation strategies, AutoAugment [3] and Cutout [4].

For CIFAR10 and CIFAR100, we applied the ResNet-18 and ResNet-19 architectures. We used a stochastic gradient descent optimizer with a momentum of 0.9 to train for 300 epochs. The initial learning rate was set to 0.1, and we employed a cosine annealing learning rate strategy. The batch size is 128, and weight decay is  $5e-4$ . Additionally, we use the QKFormer architecture to recognize static targets with the same training strategy as the original [54].

On the ImageNet dataset, we train 300 epochs using ResNet-18 with a batch size of 256. The initial learning rate value is 0.1 and the learning rate is adjusted using a cosine annealing strategy. The default input size is  $224 \times 224$ , which is consistent with other methods.

Table 10 illustrates the architectures of the VGG-9, VGGSNN, ResNet-18, and ResNet-19 models that were used in the experiment. We use the same architecture and experimental setup as in our method when we reproduce CLIF [18], TAB [19], and SLT [2], but we use the officially released core code implementation to ensure performance.

## C. Additional Experimental Results

### C.1. Comparison with Adaptive Gaussian Noise

To further demonstrate that discrete spike noise outperforms continuous Gaussian noise in SNNs, we construct adaptive Gaussian noise using the spike firing rate as its standard deviation. As shown in Table 11, our amplitude-aware spike noise still exhibits significant performance advantages over adaptive Gaussian noise.

### C.2. Further Comparison with the Baseline

The VGG-9 architecture was trained for 100 epochs by default. To show that our method consistently outperforms the baseline model rather than due to underfitting, we ex-

Table 10. Structures of VGG-9, VGGSNN, ResNet-18, and ResNet-19, where AP, GAP, and FC denote average pooling, global average pooling, and fully connected layers, respectively.

Stage	VGG-9	VGGSNN	ResNet-18	ResNet-19
1	-	-	Conv(3 × 3@64)	Conv(3 × 3@128)
1	Conv(3 × 3@64) Conv(3 × 3@128)	Conv(3 × 3@64) Conv(3 × 3@128)	$\left( \begin{array}{c} \text{Conv}(3 \times 3@64) \\ \text{Conv}(3 \times 3@64) \end{array} \right) \times 2$	$\left( \begin{array}{c} \text{Conv}(3 \times 3@128) \\ \text{Conv}(3 \times 3@128) \end{array} \right) \times 3$
	AP(stride=2)	AP(stride=2)	-	-
2	Conv(3 × 3@256) Conv(3 × 3@256)	Conv(3 × 3@256) Conv(3 × 3@256)	$\left( \begin{array}{c} \text{Conv}(3 \times 3@128) \\ \text{Conv}(3 \times 3@128) \end{array} \right) \times 2$	$\left( \begin{array}{c} \text{Conv}(3 \times 3@256) \\ \text{Conv}(3 \times 3@256) \end{array} \right) \times 3$
	AP(stride=2)	AP(stride=2)	-	-
3	Conv(3 × 3@512) Conv(3 × 3@512)	Conv(3 × 3@512) Conv(3 × 3@512)	$\left( \begin{array}{c} \text{Conv}(3 \times 3@256) \\ \text{Conv}(3 \times 3@256) \end{array} \right) \times 2$	$\left( \begin{array}{c} \text{Conv}(3 \times 3@512) \\ \text{Conv}(3 \times 3@512) \end{array} \right) \times 2$
	AP(stride=2)	AP(stride=2)	-	-
4	Conv(3 × 3@512) Conv(3 × 3@512)	Conv(3 × 3@512) Conv(3 × 3@512)	$\left( \begin{array}{c} \text{Conv}(3 \times 3@512) \\ \text{Conv}(3 \times 3@512) \end{array} \right) \times 2$	
	GAP,FC	AP,FC	GAP,FC	GAP,FC × 2

Table 11. Comparative results (%) with adaptive Gaussian noise.

Method	CIFAR10-DVS	DVS-Gesture
Adaptive Gaussian noise	73.9	88.54
<b>Ours (Amplitude-aware spike noise)</b>	<b>77.1</b>	<b>94.44</b>

Table 12. Comparative results (%) under extended training epochs.

Dataset	Method	100 Epoch	200 Epoch	300 Epoch
CIFAR10-DVS	Baseline	72.9	74.1	74.2
	<b>Ours</b>	<b>77.1</b>	<b>77.2</b>	<b>77.5</b>
DVS-Gesture	Baseline	87.15	89.58	89.58
	<b>Ours</b>	<b>94.44</b>	<b>95.14</b>	<b>95.49</b>

Table 13. Further comparative results under identical settings as MPS [6].

Dataset	Method	Architecture	$T \downarrow$	Accuracy (%) $\uparrow$
CIFAR10-DVS	MPS <sup>ICLR'25</sup> [6]	VGG-9	5	76.77
	<b>Ours</b>	VGG-9	5	<b>77.20</b>
	MPS <sup>ICLR'25</sup> [6]	VGGSNN	4	83.20
	<b>Ours</b>	VGGSNN	4	<b>83.70</b>
DVS-Gesture	MPS <sup>ICLR'25</sup> [6]	VGG-9	5	93.23
	<b>Ours</b>	VGG-9	5	<b>95.14</b>
N-Caltech101	MPS <sup>ICLR'25</sup> [6]	VGG-9	5	82.71
	<b>Ours</b>	VGG-9	5	<b>84.03</b>
	MPS <sup>ICLR'25</sup> [6]	VGGSNN	10	93.68
	<b>Ours</b>	VGGSNN	10	<b>94.25</b>

tended the training cycle to 300 epochs. The comparative results are presented in Table 12. These results demonstrate that our method consistently yields significant performance gains.

### C.3. Further Comparison with MPS

Due to MPS’s strong performance on neuromorphic datasets, Table 13 provides an additional comparison between our method and MPS [6]. This comparison ensures that all training strategies, including model architecture

Table 14. Computing consistency loss by applying the AND operation across additional layers can further enhance performance.

Dataset	Method	Architecture	$T \downarrow$	Accuracy (%) $\uparrow$
CIFAR10-DVS	Baseline	VGG-9	4	72.9
	<b>Ours</b>	VGG-9	4	<b>77.1</b>
	<b>Ours Dense</b>	VGG-9	4	<b>78.8</b>
DVS-Gesture	Baseline	VGG-9	4	87.15
	<b>Ours</b>	VGG-9	4	<b>94.44</b>
	<b>Ours Dense</b>	VGG-9	4	<b>95.49</b>

Table 15. Comparative results on static CIFAR10 and CIFAR100 datasets.

Dataset	Method	Architecture	$T \downarrow$	Accuracy (%) $\uparrow$
CIFAR10	QKFormer <sup>NeurIPS'24</sup> [54]	QKFormer	4	96.18
	SNN-ViT <sup>ICLR'25</sup> [38]	SNN-ViT	4	96.10
	RateBP <sup>NeurIPS'24</sup> [49]	ResNet-19	4	96.26
	DeepTAGE <sup>ICLR'25</sup> [25]	ResNet-18	4	95.86
	SLT <sup>AAAI'24</sup> [2]	ResNet-19	4	95.18
	LSG <sup>JCAI'23</sup> [24]	ResNet-19	4	95.17
	RateBP <sup>NeurIPS'24</sup> [49]	ResNet-18	4	95.61
	KDSNN <sup>CVPR'23</sup> [42]	ResNet-18	4	93.41
	Weak2Strong <sup>NeurIPS'25</sup> [7]	ResNet-19	4	96.66
	<b>Ours</b>	ResNet-18	4	<b>95.70</b>
	ResNet-19	4	<b>96.73</b>	
CIFAR100	QKFormer <sup>NeurIPS'24</sup> [54]	QKFormer	4	81.15
	SNN-ViT <sup>ICLR'25</sup> [38]	SNN-ViT	4	80.10
	RateBP <sup>NeurIPS'24</sup> [49]	ResNet-18	4	78.26
	STAA-SNN <sup>CVPR'25</sup> [52]	ResNet-19	4	82.05
	DeepTAGE <sup>ICLR'25</sup> [25]	ResNet-19	4	81.39
	RateBP <sup>NeurIPS'24</sup> [49]	ResNet-19	4	80.71
	TS-SNN <sup>ICML'25</sup> [51]	ResNet-19	2	80.28
	ReverB-SNN <sup>ICML'25</sup> [15]	ResNet-19	2	78.46
	TMC <sup>ICML'25</sup> [45]	ResNet-19	4	77.52
	SLT <sup>AAAI'24</sup> [2]	ResNet-19	4	75.01
	Weak2Strong <sup>NeurIPS'25</sup> [7]	ResNet-19	4	82.02
	<b>Ours</b>	ResNet-18	4	<b>78.83</b>
		ResNet-19	4	<b>82.29</b>

and timestep settings, are identical. Our method demonstrated superior performance across three datasets, consistently outperforming MPS.

#### C.4. Further Extension of the Proposed Method

By default, we only apply the AND operation to the output of the penultimate layer (before the fully connected layer) to extract the stable pulse skeleton and compute the consistency loss. Naturally, we can extend this implementation to more layers. For now, we'll call it Stable Spike Dense. To accomplish this, we treat every two convolutions in VGG-9 as a stage and compute the consistency loss by performing an AND operation on the output features of each stage. As

more layers have been optimized for consistency, the results in Table 14 indicate further performance improvements.

#### C.5. Experimental Results on CIFAR

Table 15 shows the experimental results of our method using the ResNet-18 and ResNet-19 architectures on CIFAR10 and CIFAR100. With four timesteps, we achieved accuracy rates of 96.73% on CIFAR10 and 82.29% on CIFAR100, significantly outperforming other methods.

Table 16. Hyperparameter sensitivity experiments (%) across architectures and timesteps on multiple datasets.

T=4,VGG-9, $\alpha =$	1	2	3	4	$\beta = 0.25$	0.5	0.75	1.0	1.25	1.5	$\gamma = 0.25$	0.5	0.75	1.0	1.25	1.5
CIFAR10-DVS	76.2	77.1	76.9	77.1	76.0	76.6	<b>77.3</b>	77.1	76.5	76.8	76.1	75.8	76.2	77.1	75.6	76.4
N-Caltech101	82.39	<b>83.92</b>	82.49	82.82	82.71	82.60	82.60	<b>83.92</b>	83.15	82.82	83.15	83.26	82.71	<b>83.92</b>	82.71	82.28
DVS-Gesture	93.40	94.44	<b>95.14</b>	94.10	93.75	95.04	94.10	94.44	93.75	93.40	94.10	94.10	93.06	94.44	93.75	93.06
T=16,QKFormer, $\alpha =$	1	2	3	4	$\beta = 0.25$	0.5	0.75	1.0	1.25	1.5	$\gamma = 0.25$	0.5	0.75	1.0	1.25	1.5
DVS-Gesture	98.26	<b>98.61</b>	98.26	98.26	98.26	98.26	98.61	98.61	98.26	98.26	98.26	98.26	98.26	98.61	98.26	98.61

Table 17. Optimizing consistency across all timesteps does not eliminate useful temporal information.

Consistency	CIFAR10-DVS	DVS-Gesture
<b>All timestep</b>	<b>77.1</b>	<b>94.44</b>
First two timesteps	75.2	91.67
Last two timesteps	75.9	93.06

significantly improves the inference performance of SNNs with negligible training overhead.

### C.6. Additional Hyperparameter Sensitivity Experiments

To further investigate the sensitivity of the proposed method to hyperparameters, we conducted additional experiments across architectures and timesteps on neuromorphic datasets. Table 16 shows that our method exhibits stable overall performance as long as the hyperparameters remain within reasonable ranges ( $\beta = \gamma = 1.0$  and  $\alpha = 2.0$ ). We recommend increasing  $\beta$  and  $\gamma$  appropriately when tasks exhibit significant temporal fluctuations and increasing  $\alpha$  appropriately when interclass differences are excessive to smooth out variations in probability distributions.

### C.7. Stable spikes can maintain temporal information.

**Stable spikes maintain  $T - 1$  step temporal coherence by eliminating transient noise rather than erasing all temporal information.** Legitimate temporal dynamics are essentially the ordered evolution of spatial features over time. This evolution rarely isolates the features from adjacent timesteps, thus enabling their preservation by stable spikes. Additionally, Table 17 shows that optimizing only the first and last two timesteps results in suboptimal performance. This further validates that applying our method to all timesteps does not eliminate useful temporal information, but rather enhances it.

### D. Negligible Training Overhead

Our method only requires performing the AND operation on the last layer spike maps during training. Then, forward propagation is performed with noise added. The AND bit operation and the cost of generating random noise are negligible, and forward propagation only involves one fully connected layer. Therefore, we did not observe any significant memory or time overhead during training. During inference, our method is the same as the vanilla SNN, so it does not affect inference efficiency at all. Overall, our method

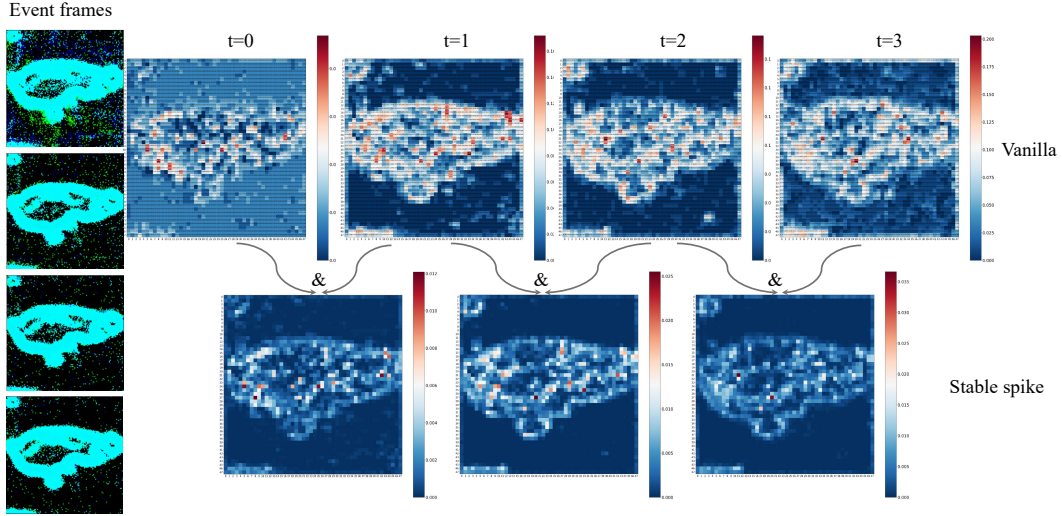


Figure 6. Visualization of the second layer spike maps of VGG-9 on CIFAR10-DVS. The stable spike maps decoupled by the minimal  $\&$  operation precisely depict the feature skeleton, echoing the results of Fig. 1 in the main paper. To ensure the visualization effect, the average of the spike maps of all channels is displayed.

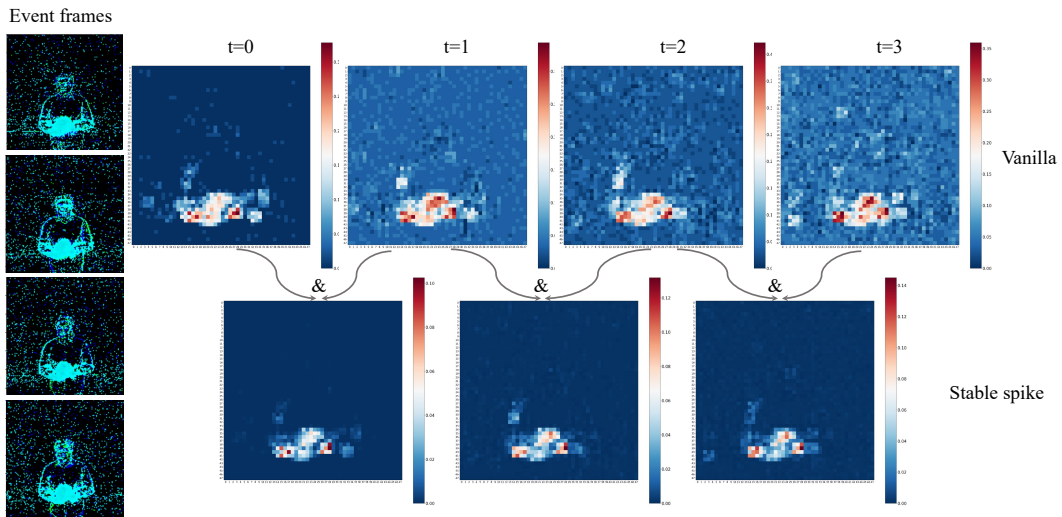


Figure 7. Visualization of the first layer spike maps of VGG-9 on DVS-Gesture. The stable spike maps decoupled by the minimal  $\&$  operation precisely depict the feature skeleton, echoing the results of Fig.1 in the main paper. To ensure the visualization effect, the average of the spike maps of all channels is displayed.

## E. Additional Visualizations

In this section, we present additional spike map visualizations to demonstrate the consistency of “the vanilla spike map differences across timesteps and the ability of the stable spike to accurately represent the feature skeleton” across multiple datasets and layers. Fig. 1 in the main paper shows the spike map of the first layer of the VGG-9 architecture on CIFAR10-DVS. Fig. 6 shows the spike map of the second layer. Fig. 7 and Fig. 8 show the spike maps of the first two layers on DVS-Gesture, respectively.

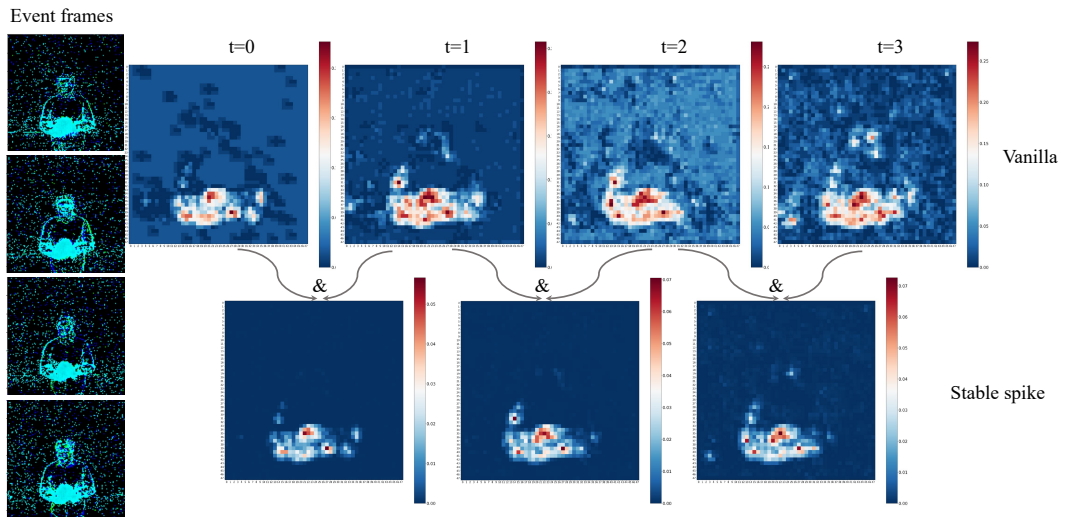


Figure 8. Visualization of the second layer spike maps of VGG-9 on DVS-Gesture. The stable spike maps decoupled by the minimal  $\&$  operation precisely depict the feature skeleton, echoing the results of Fig.1 in the main paper. To ensure the visualization effect, the average of the spike maps of all channels is displayed.